ACS APPLIED ELECTRONIC MATERIALS

pubs.acs.org/acsaelm

Article

Liquid Metal-Based Angle Detection Sensor

Fei Zhan, Peiliu Li, Jun-Heng Fu, Jiaye Zhan, Qijia Wang, Hongbin Zhao, Xinlong Sun, Shousheng Tang, Jing Liu, and Lei Wang*

Cite This: *ACS Appl. Electron. Mater.* 2023, 5, 3571−3578

Read Online

ACCESS | Metrics & More | Article Recommendations | Supporting Information

ABSTRACT: Liquid metal (LM) as the universal artificial biomimetic sensory material has attracted much interest in academic and industrial applications, such as soft robots, flexible electronics, and micro−nano devices. It remains a pivotal challenge to develop a stable and highly sensitive angle detection with a rapid response. Herein, we present an LM-based angle detection sensor. Ga-based LM is gradually injected into hollow fibers with rough internal structures, resulting in a gradient of LM content inside the fibers due to the synergistic effect of pressure drop and the fast formation of an oxide film on its surface. The LM is affected by the gravity pressure when the fiber is tilted, and the Laplace pressure on the surface of the LM continuously reaches an equilibrium state to induce the continuous deformation of the LM. The proposed sensor with highly sensitive to the tilt angle and showcases a linear relation with the tilt angle. For its advantages, this work shows a great potential application in sensor fields and opens routes for the application of electronic whiskers.

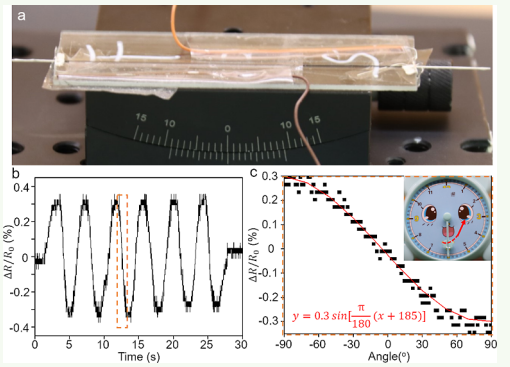

KEYWORDS: *liquid metal, Laplace pressure, angle detection sensor, tilt angle, electronic whiskers*

1. INTRODUCTION

Angle sensing is a critical technology that is indispensable in various fields. It allows for accurate measurement of angular displacement, making it essential in instrumentation and control systems for determining the position of rotating components such as motors, valves, and gearboxes. In mechanical guides, angle sensors are used to measure the orientation of a platform or the tilt of a structure, ensuring stability and safety. In the healthcare industry, angle sensors are used for detecting human joint movements, monitoring limb positions during physical therapy or rehabilitation, and evaluating treatment effectiveness. In robotics, angle sensors play a vital role in monitoring robot joint motion and ensuring precise positioning of robotic arms and other components, resulting in increased productivity and efficiency. Therefore, the development of high-precision and reliable angle sensors has become crucial to ensure the accuracy and effectiveness of these systems.[1,2] Angle sensors based on laser, electrical, and magnetic principles have been developed, which offer a large measuring range and high precision.[3−5] However, it is worth noting that these sensors tend to be both expensive and large in size.[6,7] Given the trend toward miniaturization, there is a pressing need to develop angle sensors that can be easily manufactured at a low production cost.

In recent years, LM has gained widespread use in the preparation of various sensor parts due to its attractive properties, such as fluidity and conductivity, which allow for remarkable adaptability in various applications, particularly under tensile force and pressure.[8−18] Gallium-based LM has been successfully integrated into the field of stretchable and wearable electronics. The LM generates an oxide layer that adheres to various materials, making it highly versatile. Furthermore, when the LM is subjected to mechanical deformation, the oxide layer is torn and quickly regenerated. This makes it suitable for use in various manufacturing methods such as stencil printing, 3D printing, direct writing, spray deposition, and more.[19−23] Wang et al. proposed an electronic whisker by injecting LM into the fiber.[24] He et al. proposed a spiral tubular sensor to monitor the attitude of a serpentine soft robot by detecting axial tension and curvature. Varga et al. proposed a capacitive inertial sensor based on the movement of LM droplets. Due to the adhesion of the LM oxide layer, the motion state cannot be recorded quickly and accurately.[25,26] Liu et al. induced the deformation of LM by applying an applied electric field and synergistic oxidation.[27] The high surface tension of LM means that the oxide layer of LM plays a significant role in its deformation. As LM flows inside a micropipe, friction between the LM and the pipe wall causes a pressure drop, resulting in varying amounts of LM oxide being attached to different locations on the pipe wall.

Received: February 21, 2023
Accepted: June 25, 2023
Published: July 4, 2023

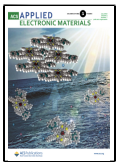

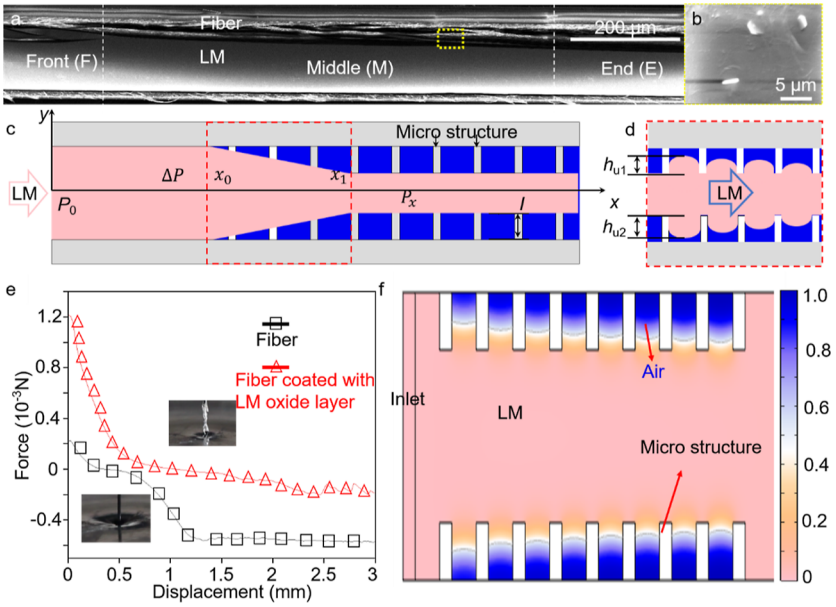

Figure 1. (a), SEM of LM in fiber. (b) Magnified view of the microstructures on the inner surface of the fiber. (c,d) Schematic diagram of LM distribution when it is injected into the fiber, blue represents air and pink represents LM, respectively. (e) Advancing resistance of fibers with and without LM. (f) Simulation of competition between air and LM in the fiber, the legend shows the volume fraction of LM and air.

The microstructure on the inner wall of the pipe can further enhance the sensitivity of LM deformation.[28−30]

Ga-based LM performs well not only in terms of electrical conductivity but also in terms of mobility. Therefore, since the LM is enclosed in a closed solid space containing an air gap, it can move inside the solid space. It will be deformed in response to external vibrations and changes in pressure, resulting in changes in electrical signals. In this study, fiber sensing based on the microrheological characteristics of LM is proposed to determine whether the equipment is in a stable state by detecting the tilt angle.

2. RESULTS AND DISCUSSION

During the process of injecting LM into a hollow fiber, residual air inside the fiber can cause gradual oxidation of the LM surface. The resulting oxide layer comes into close contact with the rough microstructure (Figure S1) and, under pressure, attaches to it, leading to a pressure drop. This gradual increase in pressure drives the LM to flow at a uniform speed inside the fiber, resulting in three different distribution states within the fiber—the front (F), middle (M), and end (E)—as shown in Figure 1a.

When LM is injected into the fiber at the same speed, the pressure on the F is larger due to the presence of a pressure drop. Consequently, the oxide layer of the LM directly attaches to the inner wall of the fiber (Figure S2). As the pressure of the LM decreases relative to the F, the oxide layer of the LM will not adhere to the inner wall of the fiber as extensively, mainly attaching to the microstructure of the inner wall of the fiber, as shown in Figure 1b. Furthermore, with the decrease of the LM pressure, the diameter of the LM on the microstructure gradually decreases. If the pressure is not enough to squeeze the LM into the microstructure gap, the oxide layer will only adhere to the top of the microstructure at the E.

As shown in Figure 1c, there is a significant reduction in the diameter of the LM inside the fiber from 187 to 133 μm, as one moves from F to E. Additionally, a moderate downward trend can be observed in the M section. This change in diameter corresponds to a transition in the state of the LM in the fiber from the Wenzel state to the Cassie state.[31,32] The adhesion of the oxide layer on the LM gradually decreases as the contact area between the LM and fiber decreases. In this study, the geometry of the fiber sensor is modeled using an axisymmetric cylindrical tube, and a theoretical model can be established from a two-dimensional case (as shown in Figure 1c). Inside the fiber, there are microstructure arrays fabricated with a height of I and a diameter of R. Initially, LM with a density of ρ is injected into one side of the fiber at a constant velocity of V. The pressure at the injection port is P_0, and the pressure inside the fiber varies with the x-coordinate

$$P_x = P_0 - x\Delta P \tag{1}$$

the pressure drop per unit length, denoted by ΔP, is described by eq 1.[33] As we move away from the injection port, the pressure on the LM decreases, resulting in a lower wetting height in the microstructure gap. The wetting height near the injection port is denoted by $I(x < x_0)$, while it is zero when the distance from the injection port is far enough $(x > x_1)$.

The region between x_0 and x_1 is referred to as the middle area (M), where the LM cannot completely penetrate the microstructure gap due to the high Laplace pressure, as shown in Figure 1d. This study analyzes the wetting height of the LM based on force balance. When the fiber is placed horizontally, the wetting height at the bottom of the microstructure will be larger than that at the top due to the effect of gravity. The wetting height at the top of the microstructure can be expressed as

$$h_{u1}(x) = \frac{P_x r - 2\gamma\cos(\pi - \theta)}{r\rho g} \tag{2}$$

where r is the radius of the microstructure gap, g is the gravitational acceleration, γ and θ are the surface tension and contact angle of LM, respectively. And the wetting height of LM at the bottom of the microstructure can be described as

https://doi.org/10.1021/acsaelm.3c00228
ACS Appl. Electron. Mater. 2023, 5, 3571−3578

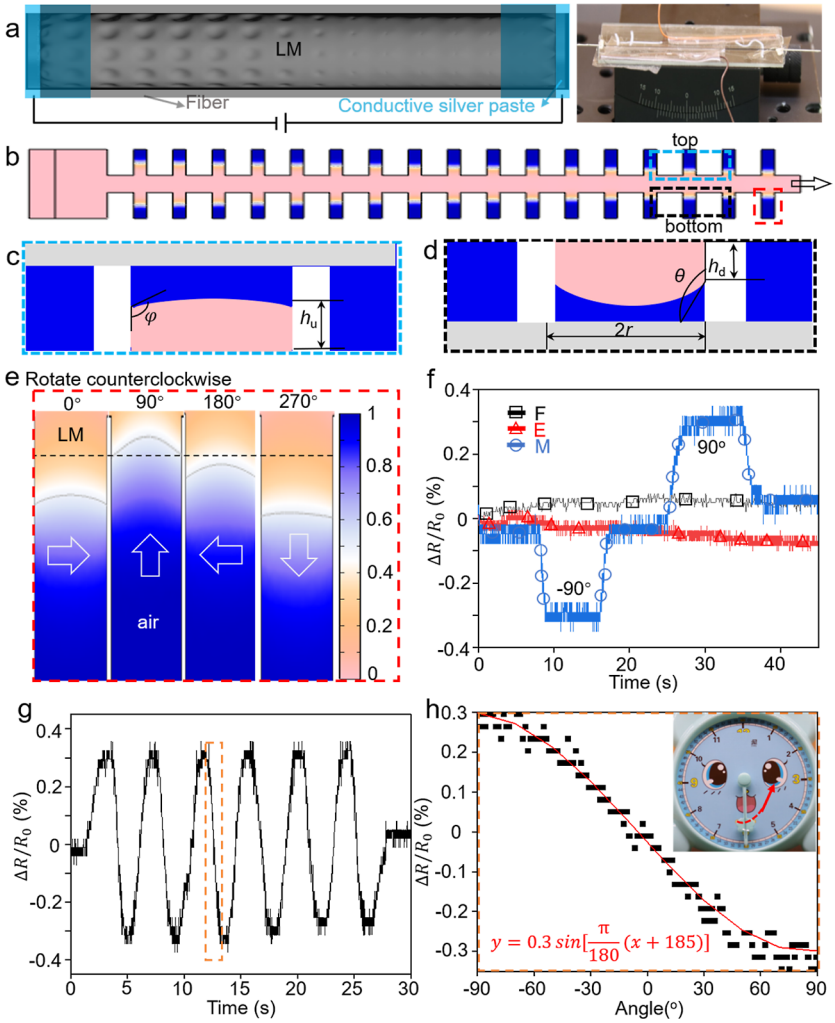

Figure 2. (a), Schematic diagram of the sensing fiber. (b) Simulation of the counterclockwise rotation of fibers. (c,d) Schematic diagram of the top and bottom of LM at the M section. (e) When the fibers are rotated 90° in turn, the wetting height of the LM in the microstructure. (f), Electrical signal of fiber at F, M, and E sections when the fiber rotates 90° sequentially. (g) Fibers rotate slowly counterclockwise from the horizontal state. (h) Electrical signal of fiber rotation from −90° to +90° and function fitting.

$$h_{u2}(x) = \frac{2\gamma\cos(\pi - \theta) - P_x r}{r\rho g} \tag{3}$$

When both the LM and the inner wall of the fiber have good wettability, the LM can easily fill the fiber completely, which blocks the deformation of the LM, and the angle sensing function is not very noticeable. In order to improve the angle sensing sensitivity, the wettability of the LM and fibers needs to be reduced. Therefore, in this study, we added graphite to the fiber preparation because graphite has poor wettability to LM. The fibers exhibited non-wetting characteristics against LM. Figure 1e shows the advancing resistance of the fiber in LM, and the fiber coated with an LM oxide layer showed better wettability with LM compared to the original fiber. The advancing resistance was reduced by 93.3% when the surface was coated with LM oxide layer. The simulation of competition between air and LM in the fiber, shown in Figure 1f, is consistent with the diagram.

After the fiber end is encapsulated with conductive silver paste and the electrode is connected, the fiber is then mounted on a glass slide. The resulting product diagram and distribution of LM within the fiber are depicted in Figure 2a. At the M section, when the injection pressure from the port is lost, the wetting height of LM in the microstructure gap changes, eventually reaching a new state of force balance as shown in Figures 2b−d.

The analysis presented above suggests that the wetting height of the LM also varies with the x-coordinate. As the x-coordinate increases, the wetting height of LM decreases, and this trend is further confirmed by simulation results (as seen in Figure 2b). The bottom and top boundaries of the wetting height of LM are illustrated in Figure 2c,d, respectively. Specifically, the wetting height of LM at the top of the microstructure can be described as

$$h_u(x) = \frac{2\gamma\cos\varphi}{r\rho g} \tag{4}$$

where φ is the receding contact angle of LM. On the other hand, at the bottom of microstructure, the wetting height can be expressed as

$$h_d(x) = \frac{2\gamma\cos(\pi - \vartheta)}{r\rho g} - R \tag{5}$$

where ϑ is the advancing contact angle of LM.[34−37] The resistance of LM inside the fiber can be described as

https://doi.org/10.1021/acsaelm.3c00228
ACS Appl. Electron. Mater. 2023, 5, 3571−3578

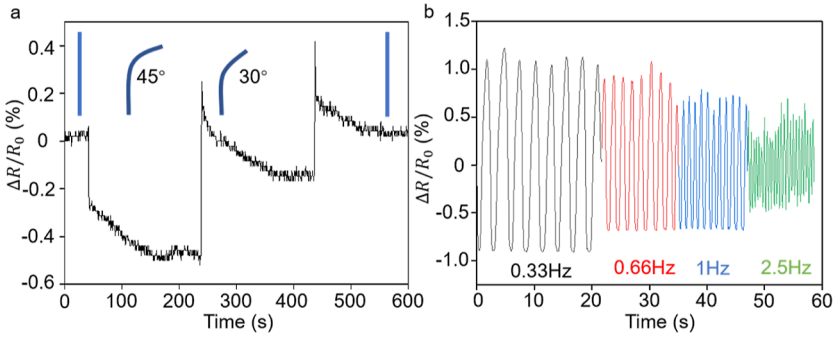

Figure 3. (a), Electrical signal when fibers bend rapidly and recover slowly. The inset shows the LM distribution when the fibers are placed upright. (b) Electrical signal when fiber rotates at different frequencies.

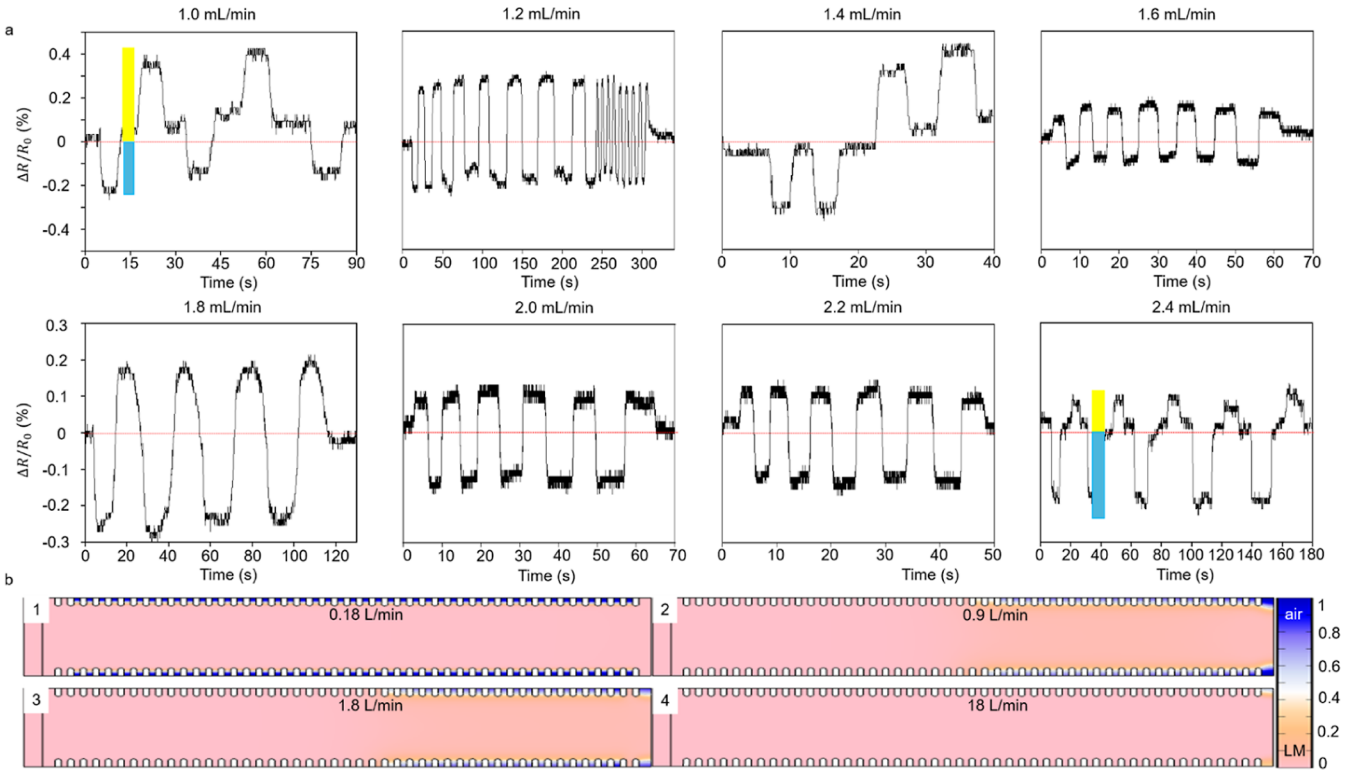

Figure 4. (a) Angle sensing demonstration with various injection speeds (1.0−2.4 mL/min). The yellow bar represents the rising range of electrical signals, and the blue bar represents the falling range of electrical signals, respectively. (b) Simulation of the distribution of LM in the fiber with different injection speeds.

$$R = \sum_{i=1}^{n} \frac{\eta X}{s_i n} \tag{6}$$

where η is the electrical conductivity of LM, and s_i is the radial cross-sectional area of LM. When the fiber rotates counterclockwise, the pressure of the LM changes due to the influence of gravity, causing the wetting height of the LM in the micro-structured gap to change continuously until it reaches a new balance at section M. Sequentially rotating the fibers counterclockwise by 90° produces a simulation of the wetting height of the LM in the micro-structured gap, as shown in Figure 2e (Movie S1), and the corresponding electrical signal change at M is shown in Figure 2f (Movies S2, S3 and S4). The LM presents a stable Wenzel state inside the fiber when the pressure of F is large enough and a stable Cassie state inside the fiber when the pressure of E is small enough. No obvious deformation of the LM occurs when the fiber rotates. The pressure of M is just enough to produce a gradient distribution in the LM, resulting in obvious electrical signal changes during rotation, indicating that M is the key factor causing the change in the electrical signal. To obtain the correspondence between angles and electrical signals, the fiber is slowly rotated counterclockwise, and its electrical signal changes are shown in Figure 2g (Movie S5). The periodic rotation produces an electrical signal that appears as a sinusoidal change. Figure 2h shows the magnified change in the electrical signal when the fiber rotates counterclockwise from −90° to +90°, and its sinusoidal fitting function can be described as

$$y = 0.3\sin\left[\frac{\pi}{180}(x + 185)\right] \tag{7}$$

In order to verify that the LM deforms under the action of gravity during the tilting process of the fiber, the fiber is quickly

https://doi.org/10.1021/acsaelm.3c00228
ACS Appl. Electron. Mater. 2023, 5, 3571−3578

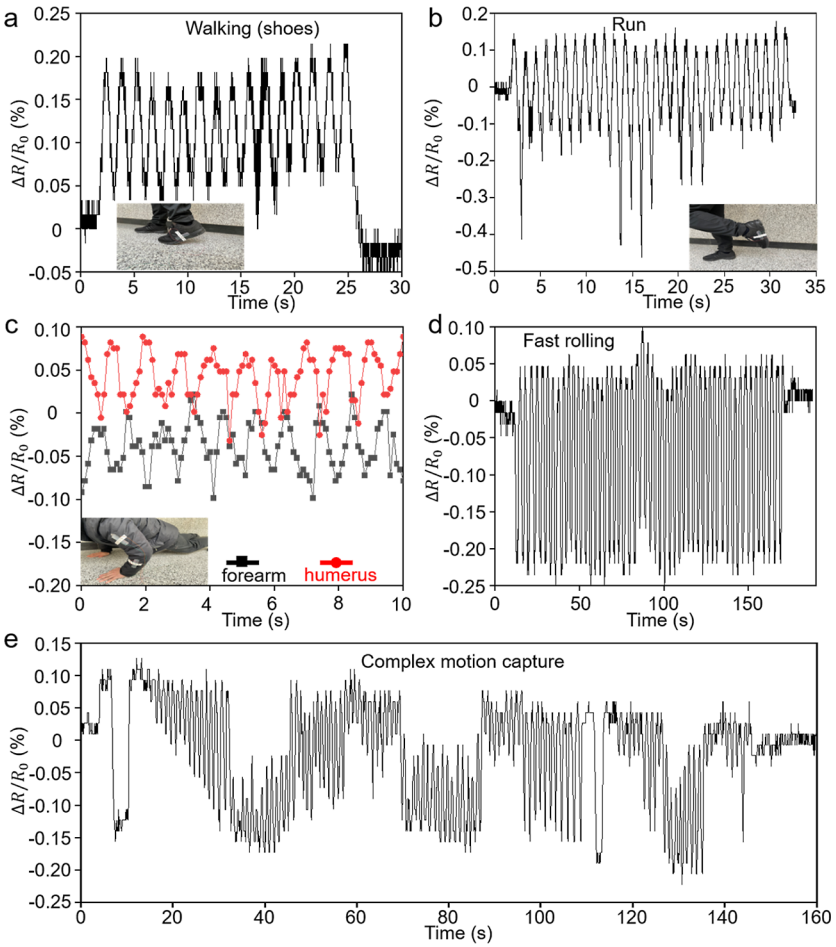

Figure 5. Detection of walking (a), jogging (b), push-ups (c), fast rolling (d), and complex motion (e).

bent by 45°, and the corresponding electronic signal becomes smaller after reaching a steady state. And then release, keep bending for 30°, the electrical signal changes slowly, then the electronic signal increases after stabilization, and finally returns to the initial vertical state. The electrical signal changes slowly and returns to the initial value after stabilization as shown in Figure 3a. This also explains the sensor's impact resistance.

As a fluid, LM causes its deformation velocity to undergo hysteresis due to its viscous characteristics.[24] Therefore, the influence of the viscosity of LM on the fiber properties through different rotation speeds is observed and shown in Figure 3b. When the rotation frequency reaches 2.5 Hz, the viscosity of LM will have a significant impact on the stability of the fiber. So, the monitoring response speed of this product can reach the highest 0.08 s/° (1 Hz).

When the fiber is tilted and rotated, the pressure of the LM inside the fiber is different under the action of gravity at different positions, and the LM overcomes the adhesion force inside the fiber and moves within the microstructure gap under the action of pressure. The flow acceleration of LM in the microstructure gap can be shown as

$$a = \frac{PS\ ^{*}\cos\omega(t) - F}{m} \tag{8}$$

where S is the cross-sectional area of the LM in the gap, ω is the rotational angular velocity, F is the adhesion of the fiber to the LM, and m is the mass of the LM in the gap. Then the flow velocity of the LM in the microstructure gap can be shown as

$$U_0 = \int_0^t a dt \tag{9}$$

When the fiber rotates from a horizontal state to a vertical state, the time required varies depending on the speed. At the same time, due to the hysteresis of the movement of LM in the microstructure gap, when the fiber rotates rapidly, the LM cannot respond quickly in a short time, which will cause the LM to fail to move to a stable position in time, so that some data are missing. The relative displacement of LM in the microstructure gap can be described as

$$X = \int_0^t U_0 dt \tag{10}$$

The pressure of the port of the fiber, which corresponds to the injection speed of the liquid metal (LM), has a significant impact on the angle sensing function as described in eq 1. This effect leads to signal migration. Figure 4a (Movies S6, S7 and S8) presents the angle detection function of the samples prepared with LM at various injection speeds. The figure shows that the zero point (indicated by the yellow-blue bar) gradually moves upward as the injection speed increases. This observation can be explained by eqs 2 and 3. Figure 4b illustrates the distribution of LM within the fiber for different injection speeds through a simulation.

The upward shift of the zero point with increasing injection speed reflects the degree of competition between the LM and air in the microstructural gap when M occupies different

https://doi.org/10.1021/acsaelm.3c00228
ACS Appl. Electron. Mater. 2023, 5, 3571−3578

positions inside the fiber. This sensing mechanism enables the fiber to be used as an angle sensor for detecting the limb behavior of the human body and the horizontal posture of a device, as shown in Figure 5.

As a non-contact angle sensor, the fiber can monitor human body movements by detecting the angle relative to the horizontal direction, as depicted in Figure 5a,b. During walking, the signal intensity is small, and the electrical signal is only present above zero. During running, the signal intensity of the electrical signal increases, and the electrical signal changes both above and below zero. By combining multiple fibers, complex signals such as push-ups, as shown in Figure 5c, can also be detected. The sensing fiber undergoes durability tests and can monitor complex motions, as demonstrated in Figure 5d (Movie S9) and Figure 5e (Movies S10 and 11). It can be used not only to monitor the steady state of aircraft but also to analyze their flight path, thus providing a novel angle detection sensor with wide applications.

3. CONCLUSIONS

In conclusion, we propose a simple and low-cost manufacturing method for angle sensors composed of LM and hollow fibers. The hollow fiber containing graphite reduces the wettability for LM, provides sufficient deformation space for LM, and increases the sensitivity of the angle sensor. In addition, we explain and illustrate the influence of the distribution state of LM inside the fiber on the angular response. The electrical signal of the fiber at different rotation speeds was tested. Based on this result, it can be inferred that the deformation response time of LM is only 0.04 s. This provides a new approach to angle sensors. It has a corrective significance for the traditional application of LM in microfluidic channels.

4. EXPERIMENTAL SECTION

4.1. Preparation of Conductive Fibers. Ga, In, and Sn are mixed at a weight ratio of 7:2:1, heated to 160 °C, stirred well for 10 min, and then cooled to room temperature. The LM was injected into the inside of a 7 cm fiber through a 5 mL syringe at a speed of 1.8 mL/min until LM flowed out from the other port of the fiber. The fibers were sealed with conductive silver paste, then they were fixed to the glass sheet; the wires were adhered to the outer wall of the fibers by the conductive silver paste; and finally, fibers were heated at 65 °C for 30 min until the conductive silver paste was dry. The fiber is achieved by hot drawing technology. PET, PBT, and graphite were mixed at a weight ratio of 49.9:49.9:0.2, heated to 260 °C, and cooled for 0.5 h. During the softening of the mixture, hot stretching techniques were applied to extrude the fibers through a microporous channel model. The fiber was obtained by rapid cooling with water at 5 °C. The graphite sheets that were not completely dispersed in the polymer solution formed rough structures on the inner and outer surfaces of the fibers.

4.2. Mechanical Properties and SEM of the Fiber. The mechanical properties of the fibers were tested by an improved force balancer system (DCA21, Dataphysics, Germany). Deformation and stress data were recorded by the software. The deformation and stress data were recorded by the software. The scanning electron microscopy (SEM) images of the fibers were observed by environmental scanning electron microscopy (Quanta FEG 250, FEI) under a voltage of 10 kV.

4.3. Simulation. COMSOL software (version 5.5) coupling the fluid mechanics, solid mechanics, and two-phase flow field modules was used to simulate the injection of LM into the fiber and the deformation of the LM inside the fiber as the fiber rotates.

■ ASSOCIATED CONTENT

Supporting Information

The Supporting Information is available free of charge at https://pubs.acs.org/doi/10.1021/acsaelm.3c00228.

SEM images of fiber inner; the distribution state and the residual state of LM; and effect of viscosity of LM on electrical signal accuracy (PDF)

Simulation of LM state in the fiber when it is tilting (MP4)

Angle sensing function at M section (MP4)

Electrical signal of fiber when the fiber rotates 90° sequentially (MP4)

Electrical signal of fiber at F, M, and E sections when the fiber rotates 90° sequentially (MP4)

Angle sensing function when the fiber is slowly rotated counterclockwise (MP4)

Angle sensor fibers with different LM injection speeds (MP4)

Angle sensing demonstration with various injection speeds (MP4)

Angle sensing demonstration with various injection speeds (MP4)

Durability tests of the sensor fibers (MP4)

Complex motion monitor of the sensor fibers (MP4)

Complex motion monitor (MP4)

■ AUTHOR INFORMATION

Corresponding Author

Lei Wang − *Beijing Key Laboratory of Cryo-Biomedical Engineering, Technical Institute of Physics and Chemistry, Chinese Academy of Sciences, Beijing 100190, China;* orcid.org/0000-0001-6674-1205; Email: leiwang@mail.ipc.ac.cn

Authors

Fei Zhan − *Beijing Key Laboratory of Cryo-Biomedical Engineering, Technical Institute of Physics and Chemistry, Chinese Academy of Sciences, Beijing 100190, China; School of Electrical and Electronic Engineering, Shijiazhuang Tiedao University, Shijiazhuang 050000, China*

Peiliu Li − *State Key Laboratory of Nonlinear Mechanics, Institute of Mechanics, Chinese Academy of Sciences, Beijing 100190, China*

Jun-Heng Fu − *College of Water Conservancy and Hydropower Engineering, Sichuan Agricultural University, Ya'an, Sichuan 625014, China*

Jiaye Zhan − *Hebei University of Technology, Tianjin 300401, China*

Qijia Wang − *Hebei University of Technology, Tianjin 300401, China*

Hongbin Zhao − *State Key Laboratory of Advanced Materials for Smart Sensing, General Research Institute for Nonferrous Metals, Beijing 100088, China;* orcid.org/0000-0003-2338-4599

Xinlong Sun − *Beijing Key Laboratory of Cryo-Biomedical Engineering, Technical Institute of Physics and Chemistry, Chinese Academy of Sciences, Beijing 100190, China*

Shousheng Tang − *Beijing Key Laboratory of Cryo-Biomedical Engineering, Technical Institute of Physics and Chemistry, Chinese Academy of Sciences, Beijing 100190, China*

https://doi.org/10.1021/acsaelm.3c00228
ACS Appl. Electron. Mater. 2023, 5, 3571−3578

Jing Liu − *Beijing Key Laboratory of Cryo-Biomedical Engineering, Technical Institute of Physics and Chemistry, Chinese Academy of Sciences, Beijing 100190, China; Department of Biomedical Engineering, School of Medicine, Tsinghua University, Beijing 100084, China;* orcid.org/0000-0002-8839-0087

Complete contact information is available at: https://pubs.acs.org/10.1021/acsaelm.3c00228

Author Contributions

F.Z. and P.L. first co-authors. L.W., H.Z., and J.L. supervised this work. F.Z. and P.L. performed the experiment and theory analysis and conducted the numerical simulations, and they are considered to be the first co-authors. F.Z., P.L., J.-H.F., J.Z., Q.W., and X.S. wrote the manuscript. S.T. and J.L. discussed the results.

Notes

The authors declare no competing financial interest.

■ ACKNOWLEDGMENTS

This work was supported by the National Natural Science Foundation of China (nos. 21805294 and 82027802).

■ REFERENCES

(1) Zhao, X.; Li, T.; Tang, Z.; Li, Y.; Miao, Y.; Xing, H.; Cai, M.; Wang, X.; Kong, X.; Ye, W. Accurate determination on the pre-tilt angle of liquid crystal cell by combining optical and electrical measurement. *Liq. Cryst.* **2021**, *48*, 15−22.

(2) Pinzón, J. R.; Estrada, T.; Happel, T.; Hennequin, P.; Blanco, E.; Stroth, U. Measurement of the tilt angle of turbulent structures in magnetically confined plasmas using Doppler reflectometry. *Plasma Phys. Controlled Fusion* **2019**, *61*, 105009.

(3) Xiaoyong, F.; Maosheng, C. Theoretical analysis of 2D laser angle sensor and several design parameters. *Opt Laser. Technol.* **2002**, *34*, 225−229.

(4) Wang, S.; Wei, X.; Weng, Y.; Zhao, Y.; Jiang, Z. A Novel Single-Axis MEMS Tilt Sensor with a High Sensitivity in the Measurement Range from 0° to 360°. *Sensors* **2018**, *18*, 346.

(5) Su, S.; Li, D.; Tan, N.; Li, G. The study of a novel tilt sensor using magnetic fluid and its detection mechanism. *IEEE Sens. J.* **2017**, *17*, 4708−4715.

(6) Zou, X.; Thiruvenkatanathan, P.; Seshia, A. A. A high-resolution micro-electro-mechanical resonant tilt sensor. *Sens. Actuators, A* **2014**, *220*, 168−177.

(7) Rao, K.; Liu, H.; Wei, X.; Wu, W.; Hu, C.; Fan, J.; Liu, J.; Tu, L. A high-resolution area-change-based capacitive MEMS tilt sensor. *Sens. Actuators, A* **2020**, *313*, 112191.

(8) Ma, J. K.; VongKong, F. M. H.; Awartani, M.; Dickey, O. M. M. D. Shaping A Soft Future: Patterning Liquid Metals. *Adv. Mater.* **2023**, *35*, 2205196.

(9) Wang, X.; Zhao, M.; Zhang, L.; Li, K.; Wang, D.; Zhang, L.; Zhang, A.; Xu, Y. Liquid metal bionic instant self-healing flexible electronics with full recyclability and high reliability. *Chem. Eng. J.* **2022**, *431*, 133965.

(10) Wu, Q.; Zhu, F.; Wu, Z.; Xie, Y.; Qian, J.; Yin, J.; Yang, H. Suspension printing of liquid metal in yield-stress fluid for resilient 3D constructs with electromagnetic functions. *npj Flexible Electron.* **2022**, *6*, 50.

(11) Kim, J.; Lee, J. Liquid-Suspended and Liquid-Bridged Liquid Metal Microdroplets. *Small* **2022**, *18*, 2108069.

(12) Peng, H.; Luo, W.; Peng, Y.; Chen, Y.; Zhang, J.; Hu, W. Plastics holding metallic conductivity via semi-liquid metals. *Sci. China Mater.* **2022**, *66*, 1124−1131.

(13) Li, X.; Li, M.; Xu, J.; You, J.; Yang, Z.; Li, C. Evaporation-induced sintering of liquid metal droplets with biological nanofibrils for flexible conductivity and responsive actuation. *Nat. Commun.* **2019**, *10*, 3514.

(14) Chang, H.; Zhang, P.; Guo, R.; Cui, Y.; Hou, Y.; Sun, Z.; Rao, W. Recoverable liquid metal paste with reversible rheological characteristic for electronics printing. *ACS Appl. Mater. Interfaces* **2020**, *12*, 14125−14135.

(15) Dong, R.; Wang, L.; Hang, C.; Chen, Z.; Liu, X.; Zhong, L.; Qi, J.; Huang, Y.; Liu, S.; Wang, L.; et al. Printed stretchable liquid metal electrode arrays for in vivo neural recording. *Small* **2021**, *17*, 2006612.

(16) Wu, Y.; Deng, Z.; Peng, Z.; Zheng, R.; Liu, S.; Xing, S.; Li, J.; Huang, D.; Liu, L. A novel strategy for preparing stretchable and reliable biphasic liquid metal. *Adv. Funct. Mater.* **2019**, *29*, 1903840.

(17) Zhou, X.; He, Y.; Zeng, J. Liquid metal antenna-based pressure sensor. *Smart Mater. Struct.* **2019**, *28*, 025019.

(18) Zhou, X.; Zhang, R.; Li, L.; Zhang, L.; Liu, B.; Deng, Z.; Wang, L.; Gui, L. A liquid metal based capacitive soft pressure microsensor. *Lab Chip* **2019**, *19*, 807−814.

(19) Zhang, J.; Zhang, C.; Li, H.; Cheng, Y.; Yang, Q.; Hou, X.; Chen, F. Controlling the oxidation and wettability of liquid metal via femtosecond laser for high-resolution flexible electronics. *Front. Chem.* **2022**, *10*, 1082.

(20) Lazarus, N.; Bedair, S. S.; Kierzewski, I. M. Ultrafine Pitch Stencil Printing of Liquid Metal Alloys. *ACS Appl. Mater. Interfaces* **2017**, *9*, 1178−1182.

(21) Bharambe, V.; Parekh, D. P.; Ladd, C.; Moussa, K.; Dickey, M. D.; Adams, J. J. Vacuum-filling of liquid metals for 3D printed RF antennas. *Addit. Manuf.* **2017**, *18*, 221−227.

(22) Neumann, T. V.; Dickey, M. D. Liquid metal direct write and 3D printing: a review. *Adv. Mater. Technol.* **2020**, *5*, 2000070.

(23) Ren, Y.; Wang, X.; Liu, J. Fabrication of high-resolution flexible circuits and sensors based on liquid metal inks by spraying and wiping processing. *IEEE Trans. Circ. Syst.* **2019**, *13*, 1545−1551.

(24) Sun, X.; Fu, J. H.; Zhao, H.; Xiang, W.; Zhan, F.; Sun, C.; Tang, S.; Wang, L.; Liu, J. Electronic whiskers for velocity sensing based on the liquid metal hysteresis effect. *Soft Matter* **2022**, *18*, 9153−9162.

(25) Zhou, L. Y.; Gao, Q.; Zhan, J. F.; Xie, C. Q.; Fu, J. Z.; He, Y. Three-dimensional printed wearable sensors with liquid metals for detecting the pose of snakelike soft robots. *ACS Appl. Mater. Interfaces* **2018**, *10*, 23208−23217.

(26) Varga, M.; Ladd, C.; Ma, S.; Holbery, J.; Tröster, G. On-skin liquid metal inertial sensor. *Lab Chip* **2017**, *17*, 3272−3278.

(27) Hu, L.; Wang, L.; Ding, Y.; Zhan, S.; Liu, J. Liquid Metals: Manipulation of Liquid Metals on a Graphite Surface. *Adv. Mater.* **2016**, *28*, 9015.

(28) Tasaka, Y.; Yoshida, T.; Murai, Y. Nonintrusive In-Line Rheometry Using Ultrasonic Velocity Profiling. *Ind. Eng. Chem. Res.* **2021**, *60*, 11535−11543.

(29) Dang, Z.; Yang, Z.; Yang, X.; Ishii, M. Experimental study on void fraction, pressure drop and flow regime analysis in a large ID piping system. *Int. J. Multiphase Flow* **2019**, *111*, 31−41.

(30) Kong, R.; Kim, S.; Bajorek, S.; Tien, K.; Hoxie, C. Effects of pipe size on horizontal two-phase flow: Flow regimes, pressure drop, two-phase flow parameters, and drift-flux analysis. *Exp. Therm. Fluid Sci.* **2018**, *96*, 75−89.

(31) Jiang, Y.; Yang, Z.; Jiang, T.; Shen, D.; Duan, J. Banana Leaf Surface's Janus Wettability Transition from the Wenzel State to Cassie−Baxter State and the Underlying Mechanism. *Materials* **2022**, *15*, 917.

(32) Liu, T.; Li, Y.; Li, X.; Sun, W. Mechanism Study on Transition of Cassie Droplets to Wenzel State after Meniscus Touching Substrate of Pillars. *J. Phys. Chem. C* **2017**, *121*, 9802−9814.

(33) Dang, Z.; Yang, Z.; Yang, X.; Ishii, M. Experimental study on void fraction, pressure drop and flow regime analysis in a large ID piping system. *Int. J. Multiphase Flow* **2019**, *111*, 31−41.

(34) Koishi, T.; Yasuoka, K.; Fujikawa, S.; Ebisuzaki, T.; Zeng, X. C. Coexistence and transition between Cassie and Wenzel state on pillared hydrophobic surface. *Proc. Natl. Acad. Sci. U.S.A.* **2009**, *106*, 8435−8440.

(35) de Hijes, P. M.; Shi, K.; Noya, E. G.; Santiso, E. E.; Gubbins, K. E.; Sanz, E.; Vega, C. The Young-Laplace equation for a solid−liquid interface. *J. Chem. Phys.* **2020**, *153*, 191102.
(36) Liu, H.; Cao, G. Effectiveness of the Young-Laplace equation at nanoscale. *Sci. Rep.* **2016**, *6*, 23936.
(37) Mo, J.; Sha, J.; Li, D.; Li, Z.; Chen, Y. Fluid release pressure for nanochannels: the Young-Laplace equation using the effective contact angle. *Nanoscale* **2019**, *11*, 8408−8415.

https://doi.org/10.1021/acsaelm.3c00228
ACS Appl. Electron. Mater. 2023, 5, 3571−3578